



LTAO End-to-End Simulation Model

Document ID: GMT-DOC-05989	Version: 1.0
Date: December 7, 2023	Status: Draft
Author(s): R. Romano and R. Conan	



Signatures

Author

Name, title

Date

Approvers

Name, title

Date

Name, title

Date



Revision Log

Version	Date	Affected Sections	Change Request #	Comments	Change Author
1.0	December 2023	7, All	None	Initial version	Author



Contents

1	Purpose	4
2	Introduction	4
3	LTAO Wavefront Control Model	6
3.1	Wavefront sensor models	6
3.2	Wavefront feedback controllers	8
3.3	Control signal transformation matrices	8
3.4	Edge sensor control loops	11
A	M2 Control System Model	15
A.1	ASM inner loop control	15
A.2	M2 positioner	17

List of Figures

1	LTAO end-to-end simulation model.	5
2	LTAO wavefront control model	7
3	LTAO sensitivity transfer functions	8
4	M1 edge sensor interaction matrix	12
5	M2 edge sensor interaction matrix.	13
6	ASM inner loop controller block diagram.	15
7	ASM segment S7 modal responses.	17
8	Frequency response magnitude of the M2 positioner actuators.	18
9	M2 positioner control loop characterization plots.	19

List of Tables

1	4 th -order Bessel filter prototype coefficients.	15
2	ASM inner loop controller model parameters	17



1 Purpose

This document describes the end-to-end model representing the Laser Tomography Adaptive Optics (LTAO) observing mode. The current version combines the LTAO wavefront control architecture and a state-space model reproducing the telescope dynamics. Though that state-space model considers a flexible face sheet representation of the ASM, at the moment, we restrict the commands to segment tip-tilt and piston. The motivation behind the LTAO model described in this effort that differs from other efforts is twofold. First, we aim to provide a first-order approximation of the laser tomographic wavefront sensor behavior, particularly regarding the limitation on measuring global tip-tilt. The second is integrating wavefront control and the loops using M1 and M2 edge sensors with other subsystem loops.

2 Introduction

Figure 1 illustrates the LTAO integrated model for end-to-end simulations. One can split the model into two parts. The first is an inner subsystem comprising a state-space model representing the telescope dynamics and low-level control loops. The second partition has the higher-level controllers relying on optical sensors. We consider low-level controllers those interfacing directly with the structural model; that is, their outputs are forces (and torques), which are inputs of the GMT structural model.

There are four low-level control loops in the current version: the mount axes (driving azimuth, elevation, and GIR drive torques), the M1 outer force loop (providing the support actuator forces), the M2 positioner, and the ASM control system. Though the M2 edge sensor (ES) control loop is not considered low-level according to the previous definition (its output is a set of offset commands handled as reference signals by the ASM controller), it is part of the M2 subsystem. Therefore, we opt to represent it within the dashed box illustrating the inner partition of the simulation model.

The mount axes control model follows ODC's design (refer to [3] for a detailed description). Each axis is controlled independently using a PID compensator and notch filters to cope with structural resonant modes. A feedforward strategy is also envisioned to relieve the feedback compensator during critical acceleration/deceleration phases. The mount control system tuning assumes a structural damping of 2%. The M1 control model implements the loop responsible for compensating for the forces acting over the mirror (measured by the hardpoint load cells) through support forces exerted by the array of pneumatic actuators. The document [8] thoroughly describes the M1 control system in the context of the GMT integrated model.

A modal control approach has been considered to improve the computational efficiency of end-to-end simulations based on the flexible face-sheet ASM design. In that approach, we apply input and output orthonormal transformations based on Karhunen-Loève (KL) modal

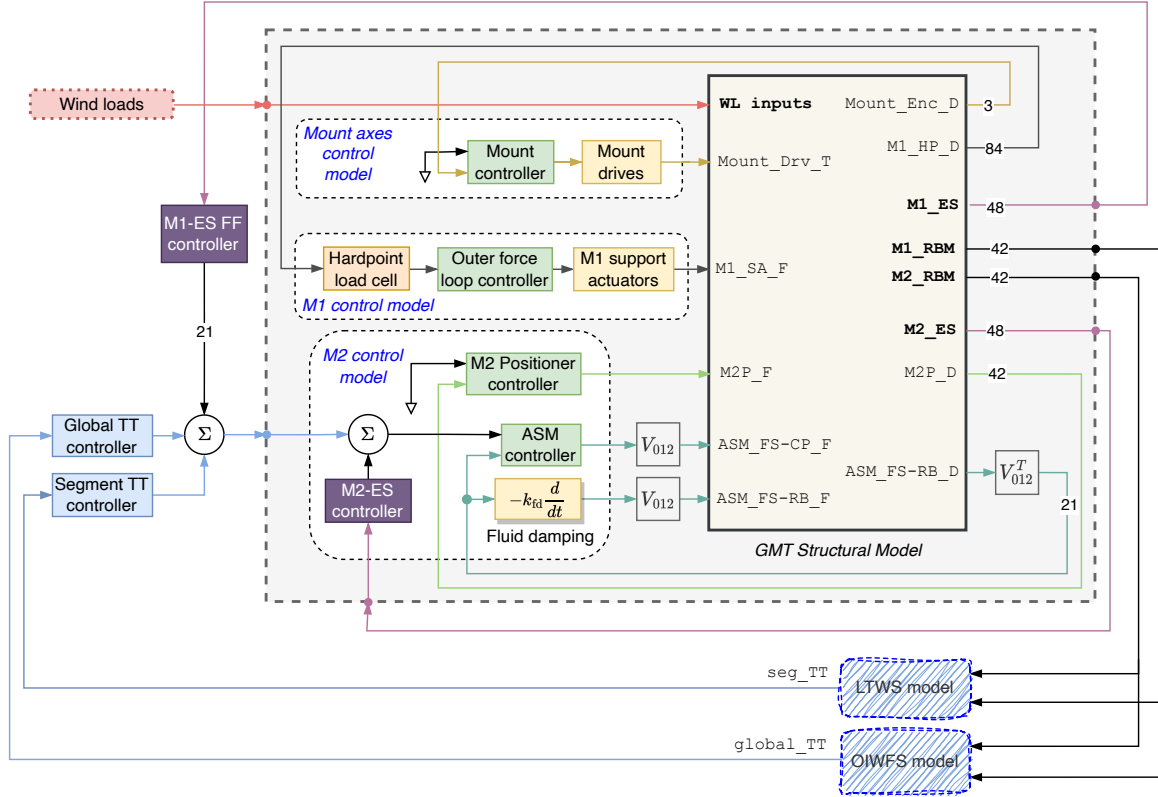


Figure 1: LTAO end-to-end simulation model.

matrix $V_{\text{KL}}^{(i)}$, which is computed according to the $n_a = 675$ coordinates of the nodes of a particular ASM segment. For each segment $i \in \{1, \dots, 7\}$, the orthonormal matrix $V_{\text{KL}}^{(i)} \in \mathbb{R}^{n_a \times n_m}$ performs the transformation from a modal basis (modal forces/modal coefficients) in the ASM KL space to a zonal basis in the ASM actuator space (actuator forces/node displacements). The transpose of $V_{\text{KL}}^{(i)}$ performs the dual transformation from a zonal basis to a modal basis. Thus, in the modal approach, modal coefficients (linear combinations of the node displacements) are fed back to the ASM inner loop controller, which outputs modal forces as control signals. The model version described in this tech note focuses on the first three KL mode shapes: piston, tip, and tilt. Therefore, $n_m = 3$ and the matrix V_{012} represented in Figure 1 reads as

$$V_{012} = \begin{bmatrix} V_{\text{KL}}^{(1)} & & \circ \\ & \ddots & \\ \circ & & V_{\text{KL}}^{(7)} \end{bmatrix}.$$



The air trapped in the thin gap between the ASM face sheet (FS) and the reference body (RB) is the source of fluid dynamic forces, which load the mirror and the reference body. Those forces are not negligible and can highly characterize the ASM system's performance and stability [4]. As shown in Figure 1, though the flexible face sheet ASM structural models have considered a wide frequency range (up to 2.1 kHz), in this document, we assume a linear fluid dynamic damping representation, with $k_{fd} = 9.1 \text{ Ns/m}$.

The M2 control system model is approached in previous documents [6, 7]. However, to make this note self-contained, we reproduce the description of the M2 control model in Appendix A.

3 LTAO Wavefront Control Model

Figure 2 provides an alternative representation of the LTAO end-to-end simulation model. The block diagram shows the controllers composing the wavefront control architecture in more detail. It also illustrates the interfaces between the high- and the low-level control loops (black dashed line block of Figure 1).

3.1 Wavefront sensor models

The linear approximations represent the Laser Tomographic Wavefront Sensor (LTWS) and the On-Instrument Wavefront Sensor (OIWFS). Let $y_{m1} \in \mathbb{R}^{42}$ and $y_{m2} \in \mathbb{R}^{42}$ vectors containing the M1 and M2 rigid-body motions, respectively. The GMT linear optical model (LOM) provides the matrices $L_{stt} \in \mathbb{R}^{14 \times 84}$, $L_{sp} \in \mathbb{R}^{7 \times 84}$, and $L_{gtt} \in \mathbb{R}^{2 \times 84}$ such that

$$\begin{bmatrix} y_{stt} \\ y_{sp} \\ y_{gtt} \end{bmatrix} = \begin{bmatrix} L_{stt} \\ L_{sp} \\ L_{gtt} \end{bmatrix} \begin{bmatrix} y_{m1} \\ y_{m2} \end{bmatrix}, \quad (1)$$

where y_{stt} , y_{sp} , and y_{gtt} are segment tip-tilt, segment piston, and global tip-tilt at the focal plane.

The tomographic wavefront sensor model provides the segment TT feedback signal. Due to the co-mounting of the lasers on the telescope and the unknown range to the sodium layer in which the guide stars are generated, one can not trust on the estimates of global tip-tilt and focus modes obtained from the LTWS. Therefore, those modes are removed from the measurements [1, 2]. Our simplified LTWS representation incorporates the global TT removal through the LOM1 block of Figure 2. In terms of ordering, assume that each of the first seven rows of L_{stt} provides the focal plane tip of a particular segment, and the last seven correspond to tilt. Thus, the linear transformation implemented in the LOM1 block is

$$L_1 = \left(I_{14} - \left(I_2 \otimes \frac{1}{7} \mathbf{1}_7 \right) \right) L_{stt},$$

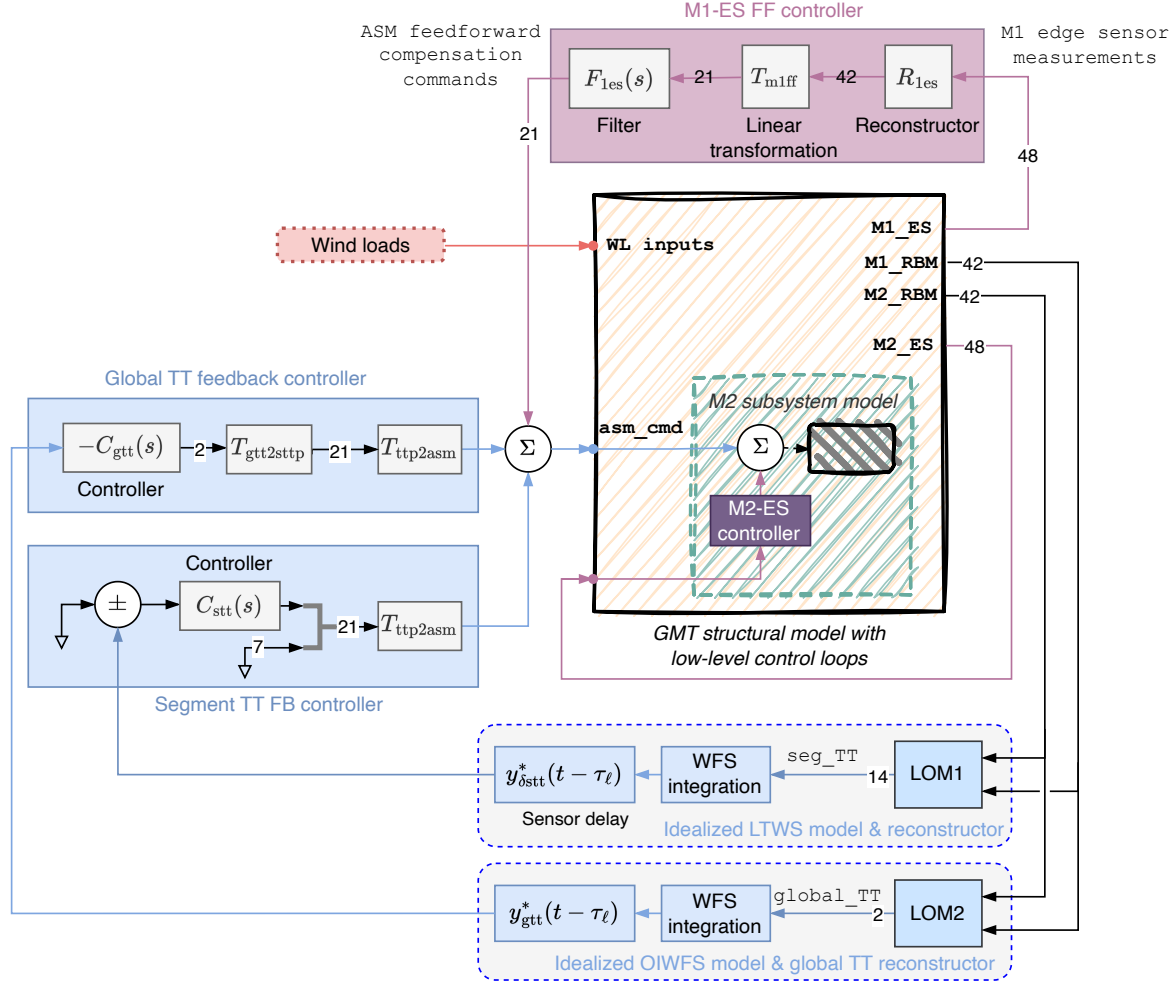


Figure 2: LTAO wavefront control system and its interfaces with the low-level control loops.

where I_n represents an n -dimensional identity matrix, $\mathbf{1}_m$ is an $m \times m$ matrix filled with ones, and “ \otimes ” denote the Kronecker product. The segment tip-tilt is obtained from

$$y_{\delta tt} = L_1 \begin{bmatrix} y_{m1} \\ y_{m2} \end{bmatrix}$$

is integrated over the $T_{ltws} = 2$ ms time window, which is also the sampling period of the feedback signal. The idealized sensor & reconstructor model also considers the sensor delay $\tau_\ell = 400 \mu s$.

In the idealized OIWFS model illustrated at the bottom of Figure 2, LOM2 indicates the



L_{gtt} transformation. As in the LTWS model, the global tip-tilt is integrated over a 2 ms time window, leading to a feedback signal sampled at the same rate. There is also a processing delay of $\tau_\ell = 400 \mu\text{s}$.

3.2 Wavefront feedback controllers

The current version does not consider the pseudo open-loop control configuration. Instead, the segment tip-tilt controller $C_{\text{stt}} = I_{14}C_{\text{ltao}}$ and the global TT compensator $C_{\text{gtt}} = I_2C_{\text{ltao}}$ are standard feedback controllers built from the same single-input single-output transfer function

$$C_{\text{ltao}}(s) = 2\pi f_c \frac{\frac{1}{2\pi f_3}s + 1}{s} \frac{s + 2\pi f_2}{s}, \quad (2)$$

with $f_c = f_2 = 32.28 \text{ Hz}$ and $f_3 = 75 \text{ Hz}$ [9].

Figure 3 shows the sensitivity transfer functions of tip-tilt and piston modes obtained with the double integrator controller (2). The plots also display the OAD requirement for the LTAO rejection transfer functions (REQ-L3-OAD-112937) [10]. The responses are within

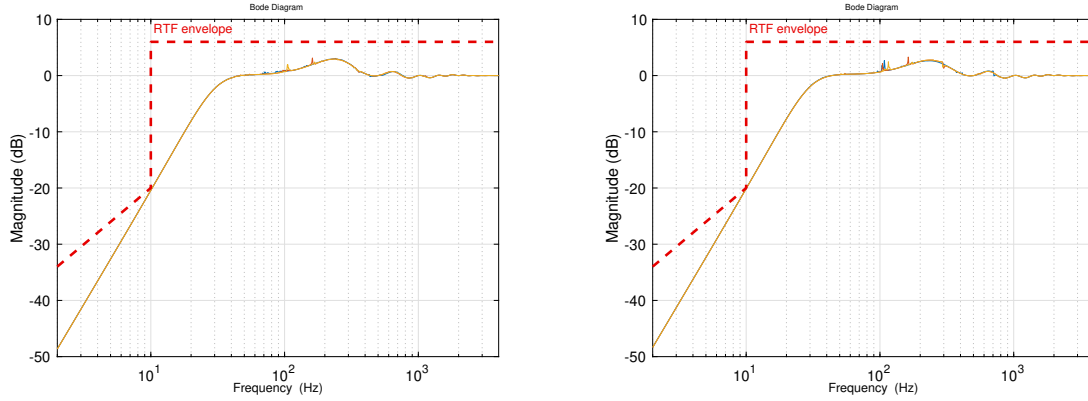


Figure 3: LTAO sensitivity transfer functions for segments S1 (left) and S7 (right-hand plot).

the requirements. Furthermore, there is almost no difference between the transfer function of segments S1 and S7 (left and right-hand plot, respectively).

3.3 Control signal transformation matrices

To map the segment and the global tip-tilt corrections calculated with C_{stt} and C_{gtt} , respectively, into ASM commands, we have used two matrices: $T_{\text{ttp2asm}} \in \mathbb{R}^{21 \times 21}$ and $T_{\text{gtt2sttp}} \in \mathbb{R}^{21 \times 2}$. The first transforms segment tip-tilt and piston at the focal plane into ASM commands represented as KL mode coefficients. In the following, the derivation of T_{ttp2asm} is approached.



Transformation from segment TT to ASM commands

Denote as $u_{\text{asm_vc}}^{(i)}$ the vector of ASM voice-coil forces¹ of a particular segment $i \in \{1, \dots, 7\}$. Using the static solution of the telescope finite-element model (FEM), we obtain the gain matrices $\bar{G}_{\text{asm_fsrb}}^{(i)} \in 675 \times 675$ and $\bar{G}_{\text{asm_rbm}}^{(i)} \in 6 \times 675$, such that

$$\begin{bmatrix} y_{\text{fs-rb}}^{(i)} \\ y_{\text{m2}}^{(i)} \end{bmatrix} = \begin{bmatrix} \bar{G}_{\text{asm_fsrb}}^{(i)} \\ \bar{G}_{\text{asm_rbm}}^{(i)} \end{bmatrix} u_{\text{asm_vc}}^{(i)} \quad (3)$$

where $y_{\text{fs-rb}}^{(i)}$ is the vector of axial displacements between pairs of nodes in the ASM face-sheet (FS) and reference body (RB) and $y_{\text{m2}}^{(i)}$ is a partition of

$$y_{\text{m2}} = \begin{bmatrix} y_{\text{m2}}^{(1)T} & y_{\text{m2}}^{(2)T} & \cdots & y_{\text{m2}}^{(7)T} \end{bmatrix}^T,$$

i.e., $y_{\text{m2}}^{(i)} \in \mathbb{R}^6$ is made up of the M2 rigid-body motions of a the i^{th} segment represented in the local coordinate system.

Consider the partitions

$$\begin{bmatrix} L_{\text{stt}} \\ L_{\text{sp}} \\ L_{\text{gtt}} \end{bmatrix} = \begin{bmatrix} L_{\text{stt.m1}}^{(1)} & \cdots & L_{\text{stt.m1}}^{(7)} & L_{\text{stt.m2}}^{(1)} & \cdots & L_{\text{stt.m2}}^{(7)} \\ L_{\text{sp.m1}}^{(1)} & \cdots & L_{\text{sp.m1}}^{(7)} & L_{\text{sp.m2}}^{(1)} & \cdots & L_{\text{sp.m2}}^{(7)} \\ L_{\text{gtt.m1}}^{(1)} & \cdots & L_{\text{gtt.m1}}^{(7)} & L_{\text{gtt.m2}}^{(1)} & \cdots & L_{\text{gtt.m2}}^{(7)} \end{bmatrix} \quad (4)$$

of the LOM matrices presented in (1) providing the contributions of each M1 and M2 segment separately. Let

$$y_{\text{mo_fs-rb}}^{(i)} = V_{\text{KL}}^{(i)T} y_{\text{fs-rb}}^{(i)} \quad (5)$$

be the ASM displacement outputs projected onto the KL modal basis and

$$u_{\text{asm_vc}}^{(i)} = V_{\text{KL}}^{(i)} u_{\text{mo_asm}}^{(i)} \quad (6)$$

the relation between the ASM voice-coil forces and its modal coefficients $u_{\text{mo_asm}}^{(i)}$. That enables us to write

$$\begin{aligned} y_{\text{sttp}}^{(i)} &\triangleq \begin{bmatrix} L_{\text{stt.m2}}^{(i)} \\ L_{\text{sp.m2}}^{(i)} \end{bmatrix} y_{\text{m2}}^{(i)} \\ &= \begin{bmatrix} L_{\text{stt.m2}}^{(i)} \\ L_{\text{sp.m2}}^{(i)} \end{bmatrix} \bar{G}_{\text{asm_rbm}}^{(i)} u_{\text{asm_vc}}^{(i)} \\ &= \begin{bmatrix} L_{\text{stt.m2}}^{(i)} \\ L_{\text{sp.m2}}^{(i)} \end{bmatrix} \bar{G}_{\text{asm_rbm}}^{(i)} V_{\text{KL}}^{(i)} u_{\text{mo_asm}}^{(i)} \end{aligned} \quad (7)$$

¹The ASM voice-coil forces are differential forces applied between nodes at the mirror face sheet and the cold plate. The input corresponding to these forces is denoted as **ASM_FS-CP_F** in Figure 1.



Thus, from the inverse of the transformation described in (7) and (3), it follows that

$$y_{\text{fs-rb}}^{(i)} = \bar{G}_{\text{asm_fsrb}}^{(i)} V_{\text{KL}}^{(i)} \left(\begin{bmatrix} L_{\text{stt_m2}}^{(i)} \\ L_{\text{sp_m2}}^{(i)} \end{bmatrix} \bar{G}_{\text{asm_rbm}}^{(i)} V_{\text{KL}}^{(i)} \right)^{-1} y_{\text{sttp}}^{(i)}$$

and then using (5) yields to

$$y_{\text{mo_fs-rb}}^{(i)} = V_{\text{KL}}^{(i)T} y_{\text{fs-rb}}^{(i)} = \underbrace{V_{\text{KL}}^{(i)T} \bar{G}_{\text{asm_fsrb}}^{(i)} V_{\text{KL}}^{(i)} \left(\begin{bmatrix} L_{\text{stt_m2}}^{(i)} \\ L_{\text{sp_m2}}^{(i)} \end{bmatrix} \bar{G}_{\text{asm_rbm}}^{(i)} V_{\text{KL}}^{(i)} \right)^{-1}}_{\triangleq T_{\text{ttp2asm}}^{(i)}} y_{\text{sttp}}^{(i)}.$$

Putting together the transformations of all segments lead to

$$T_{\text{ttp2asm}} = \begin{bmatrix} T_{\text{ttp2asm}}^{(1)} & & \bigcirc \\ & \ddots & \\ \bigcirc & & T_{\text{ttp2asm}}^{(7)} \end{bmatrix}. \quad (8)$$

Transformation from global TT to ASM commands

As the mapping from segment tip-tilt and piston (TTP) at the focal plane to the ASM displacements is available, instead of directly obtaining the ASM commands required to compensate global TT modes, as suggested in Figure 2, we split that task into two steps. First, the transformation $T_{\text{gttp2sttp}}$ relating global TT and segment TTP is addressed. Then, we use (8) to obtain the ASM compensation commands.

Consider the matrices

$$\Phi_{\text{m1m2}} = \begin{bmatrix} C(\text{m1_rbm_idxs}, 1:3) \\ C(\text{m2_rbm_idxs}, 1:3) \end{bmatrix} \in \mathbb{R}^{84 \times 3} \quad (9)$$

and

$$\Phi_{\text{AzEl}} = \begin{bmatrix} \frac{1}{n_{\text{az_enc}}} \sum_{i=1}^{n_{\text{az_enc}}} C(\text{az_enc}_i \text{idx}, 1:3) \\ \frac{1}{n_{\text{el_enc}}} \sum_{i=1}^{n_{\text{el_enc}}} C(\text{el_enc}_i \text{idx}, 1:3) \end{bmatrix} \in \mathbb{R}^{2 \times 3} \quad (10)$$

built from the first three modes of the output matrix of the telescope structural model represented in the second-order modal state-space form. The constants $n_{\text{az_enc}}$ and $n_{\text{el_enc}}$ denote the number of mount azimuth and elevation encoders, respectively, while $\text{az_enc}_i \text{idx}$ and $\text{el_enc}_i \text{idx}$ stand for the indexes of the i -th encoder in the output matrix C .

Using (9) and (10), one gets

$$T_{\text{mnt2m12}} = \Phi_{\text{m1m2}} \Phi_{\text{AzEl}}^\dagger \quad (11)$$



mapping mount azimuth and elevation motions into M1 and M2 rigid-body motions and

$$T_{\text{gtt2mnt}} = (L_{\text{gtt}} T_{\text{mnt2m12}})^{-1} \quad (12)$$

relating global tip-tilt at the focal plane and the mount axes motion. The symbol “ \dagger ” represents the Moore–Penrose inverse.

From (1) and (11)–(12), we get

$$\begin{aligned} T_{\text{gtt2sttp}} &= \begin{bmatrix} L_{\text{stt}} \\ L_{\text{sp}} \end{bmatrix} T_{\text{mnt2m12}} T_{\text{gtt2mnt}} \\ &= \begin{bmatrix} L_{\text{stt}} \\ L_{\text{sp}} \end{bmatrix} \Phi_{\text{m1m2}} \Phi_{\text{AzEl}}^{\dagger} \left(L_{\text{gtt}} \Phi_{\text{m1m2}} \Phi_{\text{AzEl}}^{\dagger} \right)^{-1}. \end{aligned} \quad (13)$$

Remark 1 *Obtaining the relation between global and segment tip-tilt is not straightforward. To avoid pseudo-inverses of matrices with more rows than columns (leading to undetermined solutions), we exploit the kinematic relations embedded into the telescope structural model represented in the state-space form through matrices (A, B, C) . In summary, the first three structural model eigenmodes reflect the dynamics of all three axes (AZ, EL, and GIR) without flexible forms. Therefore, we can use (9) and (10) relating the first three eigenmodes with M1 and M2 rigid-body motions and with the azimuth and elevation axes displacements, respectively, to get the kinematic relation (11) between the mount pointing (AZ and EL) and the M1 and M2 rigid-body motions. At last, one combines the optical sensitivity matrices (1), the kinematic relation (11), and the bijective relation (12) between global tip-tilt and mount pointing (azimuth and elevation) to develop T_{gtt2sttp} in (13).*

3.4 Edge sensor control loops

Figure 2 shows that three blocks comprise the M1 feedforward (FF) control model: the reconstructor of the M1 rigid-body motions, a linear transformation, and a filter.

Denote as $D_{\text{1es}} \in \mathbb{R}^{48 \times 42}$ the interaction matrix relating the M1 rigid-body motions and the 48-dimensional vector of distances between collimator and retro-reflector edge sensor nodes (Figure 4). An ideal linear reconstructor is the pseudo-inverse of D_{1es} . However, the edge sensors can not measure the global displacements of the M1 segments, meaning that D_{1es} is rank deficient, as shown in the right-hand plot of Figure 4 (refer also to [2] or [5, Section 4.1]). Among the available strategies to deal with rank deficiency, we have followed one of the strategies proposed in [2, Section 2.2]: inverting the truncated singular value decomposition (SVD) of the interaction matrix. So, given the decomposition

$$D_{\text{1es}} = U_{\text{1es}} \Sigma_{\text{1es}} V_{\text{1es}}^T,$$

and discarding the contribution of the six smallest singular values (corresponding to the global translations and rotations modes), the reconstructor estimating the M1 rigid-body motions



from the edge-sensor measurements reads² as

$$R_{1es} = V_{1es}(1:42, 1:36) (\Sigma_{1es}(1:36, 1:36))^{-1} (U_{1es}(1:48, 1:36))^T. \quad (14)$$

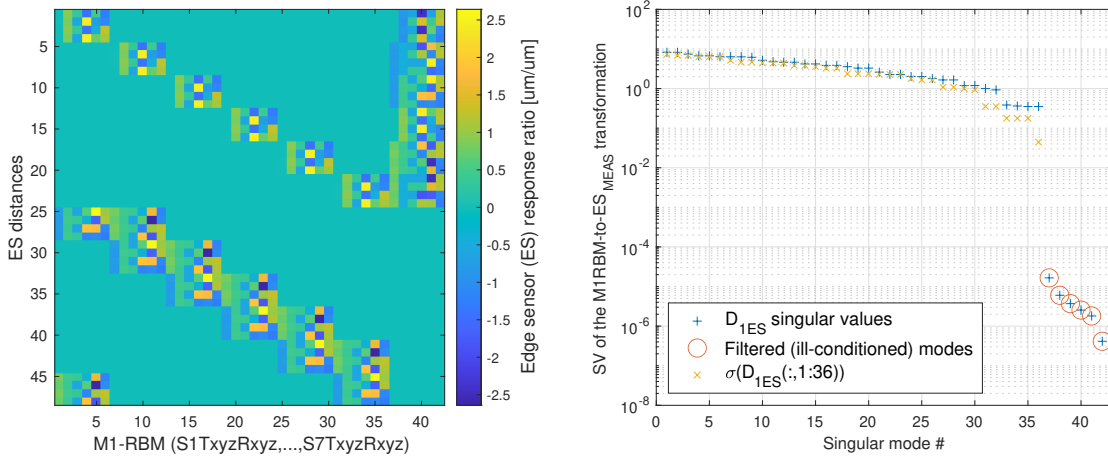


Figure 4: M1 edge sensor interaction matrix (left) and its singular values (right).

From (4) and (8), the matrix projecting the reconstructed rigid-body motions onto ASM tip-tilt and piston commands is

$$T_{m1ff} = T_{ttp2asm} \begin{bmatrix} L_{stt_m1}^{(1)} & \cdots & L_{stt_m1}^{(7)} \\ L_{sp_m1}^{(1)} & \cdots & L_{sp_m1}^{(7)} \end{bmatrix}. \quad (15)$$

The transfer function $F_{1es}(s)$ represents a second-order Butterworth filter with corner frequency set at 50 Hz. The low-pass filter follows the model used to represent the edge sensor in the M2 subsystem [4].

The M2 edge sensor control loop is part of AdOptica's design. Here, we assume the same strategy of the M1 feedforward control illustrated in Figure 2: a linear controller composed of a reconstructor R_{2es} , a linear transformation T_{m2ff} , and a 50 Hz low-pass Butterworth filter F_{2es} . On the left, Figure 5 shows the M2 edge sensor interaction matrix D_{2es} and its singular values on the right-hand plot. Therefore, analogously to (14)–(15), it follows that

$$R_{2es} = V_{2es}(1:42, 1:36) (\Sigma_{2es}(1:36, 1:36))^{-1} (U_{2es}(1:48, 1:36))^T,$$

²For compactness, we have used MatLab notation to represent blocks of matrices. For example, $V_{1es}(1:42, 1:36)$ stands for a submatrix with the first 42 rows and the first 36 columns of V_{1es} .

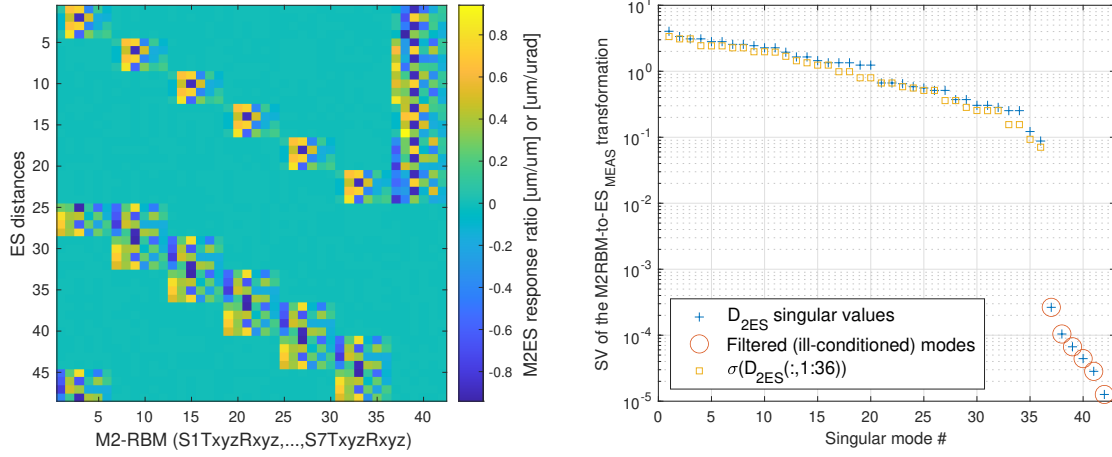


Figure 5: M2 edge sensor interaction matrix.

where $D_{2es} = U_{2es} \Sigma_{2es} V_{2es}^T$ is the matrix mapping the rigid motions of the M2 reference bodies into the 48-dimensional vector of the edge sensor distance measurements, and

$$T_{m2ff} = T_{ttp2asm} \begin{bmatrix} L_{stt_m2}^{(1)} & \cdots & L_{stt_m2}^{(7)} \\ L_{sp_m2}^{(1)} & \cdots & L_{sp_m2}^{(7)} \end{bmatrix}.$$

References

- [1] A. Bouchez et al. *GMT Wavefront Control Design Description*. Tech. rep. GMT-DOC-05023. GMTO, Sept. 2022.
- [2] Marcos van Dam et al. *M1 edge sensors in laser tomography adaptive optics*. Tech. rep. FWN 124. Flat Wavefronts, May 2022.
- [3] Alex Ippa. *End-To-End Model Description*. Tech. rep. GMT25-ANA-40000-0007. OHB Digital Connect GmbH / Ingersoll Inc., Feb. 2021.
- [4] M. Manetti et al. *GMT ASMS Phasing System Analysis Report*. Tech. rep. ADP-GASM-190-01. AdOptica, Mar. 2021.
- [5] F. Quirós-Pacheco and D. Schwartz. *GMT Segment Phase Piston Windshake Rejection with Edge Sensors*. Technical Report GMT-DOC-03396. Version 4. Giant Magellan Telescope Organization, 2019.
- [6] R. Romano. *ASM face sheet chattering behavior in dual-rate wavefront control simulations*. Tech. rep. GMT-DOC-05553. GMTO, Oct. 2022.



- [7] R. Romano. *ASM segment modal transfer function*. Tech. rep. GMT-DOC-05941. GMTO, Sept. 2023.
- [8] R. Romano, R. Conan, and C. Dribusch. *Feedback M1 Control Under the GMT Integrated Model Perspective*. Tech. rep. GMT-DOC-05153. GMTO, Oct. 2021.
- [9] P. Thompson. *Simulink IM model with NGAO controller*. [IM/Christoph/Peter/mfiles_peter/sm_20210611r.mat](#). July 2022.
- [10] B. Walls et al. *GMT Observatory Architecture Document*. Tech. rep. GMT-REQ-03215. Rev. H. GMTO, 2022.



A M2 Control System Model

A.1 ASM inner loop control

Figure 6 illustrates the ASM inner loop controller model. An input shaping filter block, a feedback compensator, and a feedforward term compose the ASM inner loop controller of each segment.

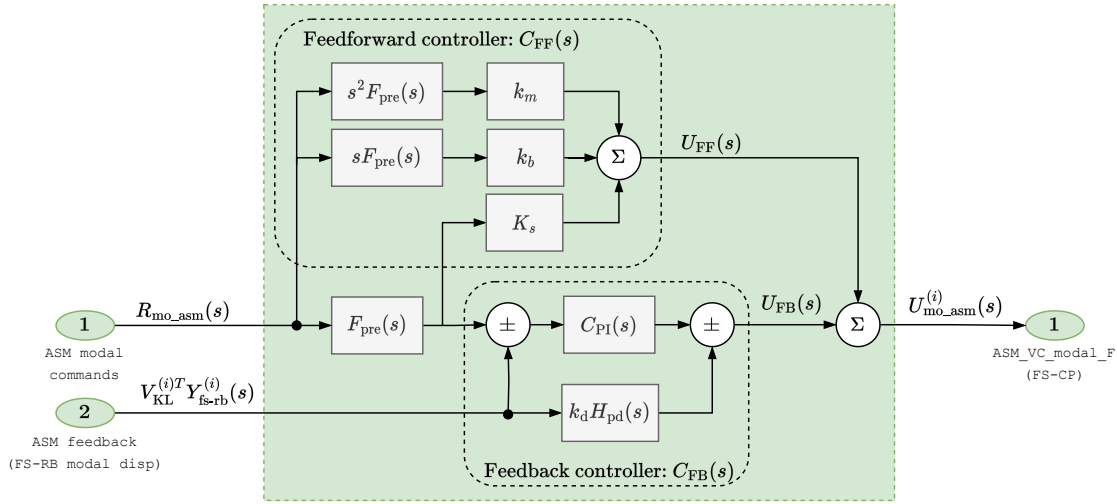


Figure 6: ASM inner loop controller block diagram.

Using a 4th-order Bessel filter with corner frequency $\omega_{\beta f} = 2\pi 2.2 \times 10^3 \text{ rad/s}$ the command pre-shape

$$F_{pre}(s) = \frac{\beta_0 \omega_{\beta f}^4}{\beta_4 \omega_{\beta f}^0 s^4 + \beta_3 \omega_{\beta f}^1 s^3 + \beta_2 \omega_{\beta f}^2 s^2 + \beta_1 \omega_{\beta f}^3 s + \beta_0 \omega_{\beta f}^4} \quad (16)$$

aims at smoothing the n_m -dimensional modal command vector $R_{mo_asm}(s)$. Table 1 provides the filter prototype coefficients β_l , for $l = \{0, 1, \dots, 4\}$.

Table 1: 4th-order Bessel filter prototype coefficients.

β_4	β_3	β_2	β_1	β_0
1.0	3.12393994	4.39155033	3.20108587	1.0

A proportional–integral compensator

$$C_{PI}(s) = I_{n_m} \left(k_p + \frac{k_i}{s} \right)$$



and derivative action proportional to k_d compose the feedback controller

$$C_{\text{FB}}(s) = -C_{\text{PI}}(s) + k_d H_{\text{pd}}(s)$$

where the transfer function

$$H_{\text{pd}}(s) = I_{n_m} \frac{s}{2\pi f_{\text{cpd}} s + 1},$$

performs a filtered differentiation with $f_{\text{cpd}} = 4\text{kHz}$. The feedback signal is the vector of relative displacements between the face sheet (FS) and the reference body (RB) nodes $y_{\text{fs-rb}}$ projected onto the orthonormal base $V_{\text{KL}}^{(i)T}$, the same signal used to model the fluid damping forces (see Figure 1).

For each ASM segment, the Laplace transform of the feedforward compensation is

$$U_{\text{FF}}(s) = \underbrace{K_s F_{\text{pre}}(s) R_{\text{mo.asm}}(s)}_{\text{static}} + \underbrace{(k_b H_{f1d}(s) + k_m H_{f2d}(s)) R_{\text{mo.asm}}(s)}_{\text{dynamic}}, \quad (17)$$

where $K_s \in \mathbb{R}^{n_m \times n_m}$ is the modal stiffness matrix Ψ_V , I_{n_m} denotes the identity matrix of dimension n_m , and

$$\begin{aligned} H_{f1d}(s) &= s I_{n_m} F_{\text{pre}}(s) \\ H_{f2d}(s) &= s^2 I_{n_m} F_{\text{pre}}(s). \end{aligned}$$

The mass k_b and the damping k_m factors are scalar gains.

Consider the $n_a \times n_a$ matrix relating the relative nodal displacements (`ASM_FS-RB_delta_D` output) due to relative nodal forces (`ASM_FS-CP_delta_F` input), denoted as $\bar{G}_{\text{asm.fsrB}}$ in (3). The modal ASM stiffness matrix for a particular segment $i \in \{1, 2, \dots, 7\}$ is

$$\Psi_V = \left(V_{\text{KL}}^{(i)T} \bar{G}_{\text{asm.fsrB}} V_{\text{KL}}^{(i)} \right)^{-1}. \quad (18)$$

One can exploit linear system realization theory to obtain the transfer functions $sF_{\text{pre}}(s)$ and $s^2 F_{\text{pre}}(s)$ in (17) without explicitly performing time-derivative operations. Consider the tuple (A_f, B_f, C_f) representing the 4th-order Bessel filter transfer function (16) in the state-space form, such that

$$F_{\text{pre}}(s) = C_f (sI_4 - A_f)^{-1} B_f. \quad (19)$$

It follows that the (filtered) ASM velocity and acceleration command transfer functions can be written as

$$sF_{\text{pre}}(s) = (C_f A_f) (sI_4 - A_f)^{-1} B_f \quad (20)$$

$$s^2 F_{\text{pre}}(s) = (C_f A_f^2) (sI_4 - A_f)^{-1} B_f. \quad (21)$$



Table 2 summarizes the ASM controller model parameter values. Figure 7 shows the ASM open- (left) and closed-loop (right) responses of segment S7 for the first three KL modes. On the right-hand plot, we also indicate the 800 Hz bandwidth requirement [10, REQ-L3-OAD-35459]. Those modal frequency responses [7] were calculated using the structural model 20230131_1605_zen_30...202111 and considering 0.5% structural damping.

Table 2: ASM inner loop controller model parameters [4].

k_p (N/m)	k_i (N/ms)	k_d (Ns/m)	k_m (Ns ² /m)	k_b (Ns/m)	K_s (N/m)
7×10^4	5×10^5	24.5	1.12×10^{-2}	33.6	Ψ_V (see (18))

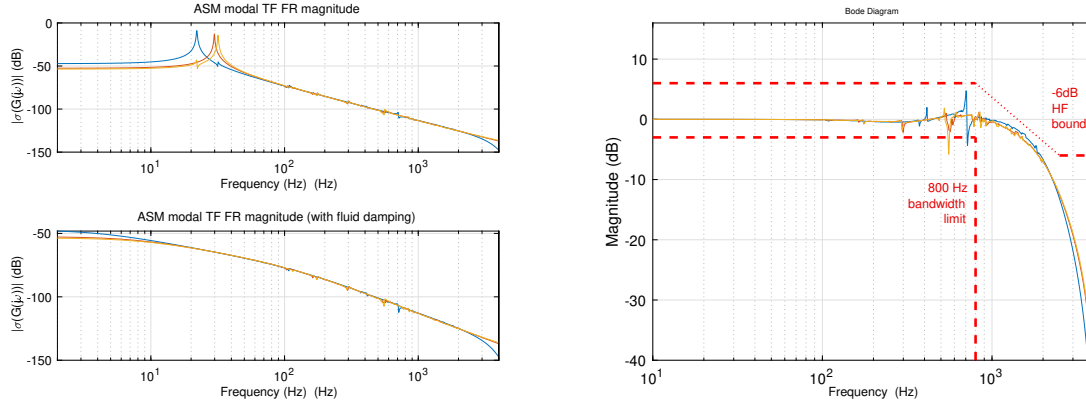


Figure 7: Adaptive secondary mirror open- and closed-loop responses.

A.2 M2 positioner

The Observatory Requirement Document (OAD) [10] stipulates through REQ-L3-OAD-35039 that the M2 positioner (M2P) shall provide a bandwidth of 2 Hz while tracks the rigid-body motion commands.

The M2P controller computes the differential forces (M2P_F), which lengthen or shorten the positioner actuators. Their lengths are the control loop feedback signals. The lengths of the M2P actuators are obtained from differential displacements of the nodes located at the extremes of the rod representing each actuator M2P_D. The frequency response magnitude of the transfer functions from M2P_F to M2P_D, denoted hereafter as $G_{m2p}(s)$, are shown in Figure 8. At the frequency range relevant for the specified closed-loop bandwidth, the model behaves like a static gain equal to the reciprocal of the stiffness of the M2P actuators, which is $k_{m2p} = 158 \text{ N/um}$. To provide enough gain at low frequencies and attenuate the modes above

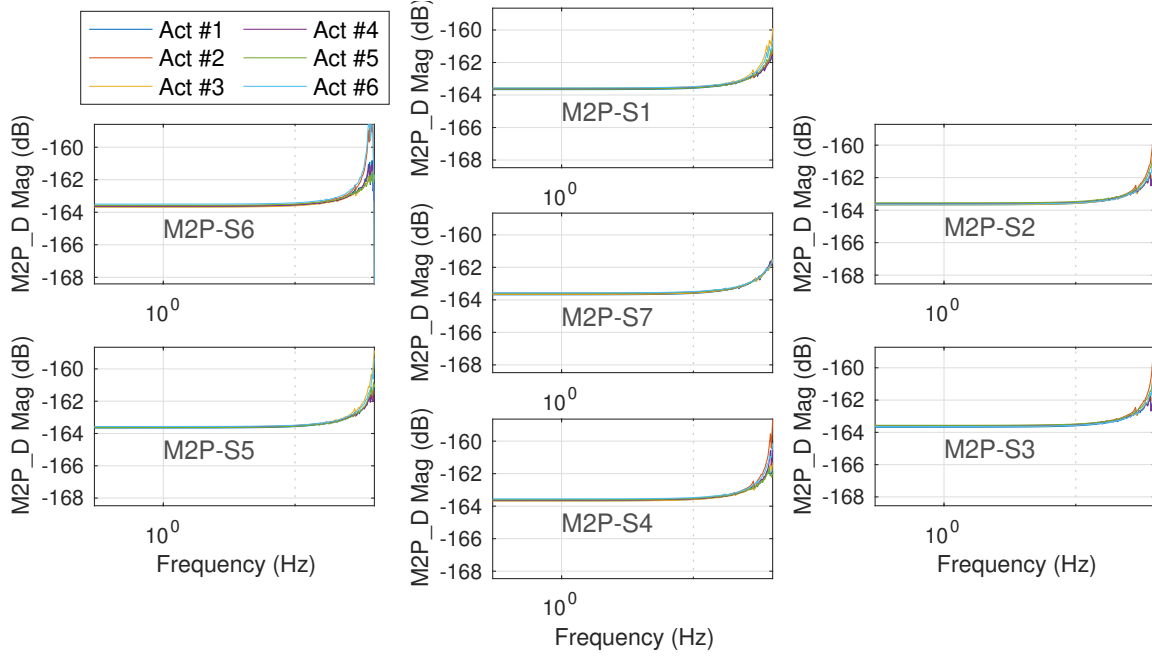


Figure 8: Frequency response magnitude of the M2 positioner actuators.

20 Hz, we use an M2P feedback controller with an integral term and a low-pass filter with a corner frequency at 10 Hz, i.e.,

$$C_{m2p}(s) = I_{42} \frac{k_{im2p}}{s} \frac{1}{\frac{1}{(2\pi 10)^2} s^2 + \frac{1}{2\pi 10} s + 1}, \quad (22)$$

where I_{42} is a 42-dimensional identity matrix and the assumed integral gain $k_{im2p} = 2\pi 2k_{m2p}$ leads to a unitary magnitude crossover frequency of 2 Hz, i.e.,

$$|G_{m2p}(j\omega_0)C_{m2p}(j\omega_0)|_{\omega_0=2\pi 2} = I_{42}.$$

The Nichols chart on the right side of Figure 9 shows quite comfortable margins as the loop frequency response is distant to the dashed red line, which indicates the robustness boundary assuming a 0.5 vector margin³ (VM). On the right side, one can see the closed-loop (complementary sensitivity) response of all the M2 positioner actuators. The control loop achieves the required bandwidth of 2 Hz using the proposed feedback controller.

³The vector margin (VM) is the reciprocal of the maximum value of the loop sensitivity transfer function $S(j\omega)$ magnitude, i.e.

$$VM = \frac{1}{\max |S(j\omega)|}.$$

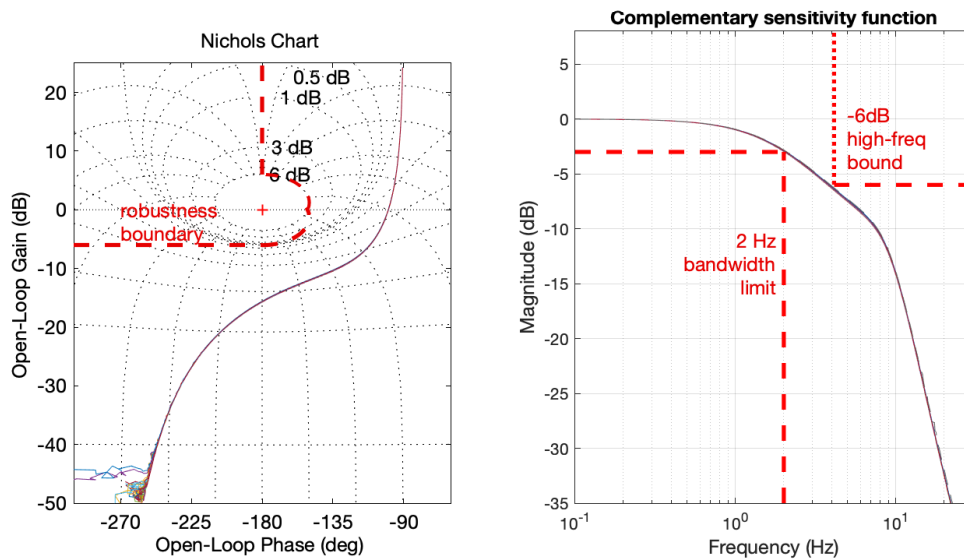


Figure 9: M2 positioner control loop characterization plots.